Scanning Laser Doppler Velocimeter System Simulation for Sensing Aircraft Wake Vortices

J. A. L. Thomson* and J. C. S. Meng†
Physical Dynamics, Inc., Berkeley, Calif.

The objectives of this study are to simulate the responses of the Scanning Laser Doppler Velocimeter System (SLDVS) in a vortex wake environment and to display the spatial signatures. From analysis of these signatures and future parallel processing of flight data and simulated data, optimal detection tactics can be established. A hydrodynamic model is developed that represents the trailing vortex sheet and wind shear as discrete free vortices distributed over a two-dimensional grid. Fast Fourier transform techniques are used to solve the vorticity stream function. The effects of buoyant exhaust and atmospheric stratifications can be incorporated in the Boussinesq approximation; the atmospheric turbulence can be simulated by constructing specific realization. A realization of Kolmogoroff's law is formulated here. Output of this model is a time-dependent, two-dimensional flowfield required for sensor analysis. A sensor model is formulated with parameters chosen to represent the NASA/MSFC SLDVS. It scans both in range and in angle to produce a fan beam configuration. The system is a coaxial, focused CO_2 laser system with Gaussian apodization. The finite truncation of the telescope mirror is accounted for by degrading the range resolution. Doppler shift is discretized at 0.545 mps per channel. No frequency translation was applied. Output of this model is a frequency spectrum vs both range and angle. Patterns of various features of the signature are presented in range-elevation angle plots. The problem of locating the vortex centers is discussed both as a pattern recognition problem and as a "point" target problem.

I. Introduction

THE implementation of reliable, efficient, and safe control of the air traffic in the airport terminal environment requires detailed knowledge of the wind shear fields in the vicinity of the airport and, in particular, in wakes of the larger aircraft. These wakes following the aircraft bear characteristics of the aircraft's weight, wing span and configuration, approach speed and height, engine configuration, engine exhaust buoyancy and thrust, as well as environmental characteristics: vertical wind shear, turbulence level, and atmospheric stability. In this report we describe a model that simulates the interaction of a laser-doppler velocimeter with the wake flowfield. This combined model of the wake and the detector system is expected to be useful both in the design of detection systems and in analyzing or correlating test data.

For simple wings the lift force is distributed elliptically (to a good approximation) along the wing so that the maximum circulation shed per length (the spanwise derivative of the lift) is at the wing tip. Hence, the maximum upwash velocity is also at the tip, and roll-up occurs there first and extends toward the fuselage. Since the maximum vorticity is at the tip, most of the vorticity shed by the wing is relatively quickly concentrated into a tip vortex. Many previous analyses were based upon the approximation that the trailing vortex sheet can be represented by two well-defined counter rotating cylindrical "tip vortices."

All of the detection systems presently considered rely specifically on such a model of the flowfield in order to reduce the vortex locations. One of the prime objectives of the LDV (Laser Doppler Velocimeter) system is to provide spatially-resolved velocity fields. However, even here finite range resolution limits the location accuracy. In order to be able to assess and develop an optimal design, a hydrodynamic model is developed that provides a reasonably realistic description of the wind-shear field; in particular, it is capable of treating nonsimple wing loadings (i.e., general flap configuration), the early time period before wrap-up, the vertical wind shear, simulated atmospheric turbulence, interaction of multiple wake vortex regions, buoyant and stratification effects of the ambient atmosphere and of the engine exhaust gases.

When the buoyancy of the exhaust gases and of the ambient atmosphere is included, the vertical motion of the wake is modified at late time. Characteristic times for stratification effects are measured by the Brünt-Väisälä time ($\tau = [T_P/(g\partial T_P/\partial z)]^{1/2}$, where T_P is the potential temperature), and are typically several minutes in the lower atmosphere.

In the presence of a finite wind, the transport phenomena will further be complicated by a shearing effect of the atmospheric turbulent boundary layer. In addition to simple convection of the wake by the wind, the wind shear is expected to alter the relative motion of the two vortices. From observation, it is known that the downwind vortex often rises.

All the physical phenomena mentioned above – the vortex sheet, ground images, the wind profile and turbulence, the buoyant exhaust and vertical stratification – are modeled in the current analysis in two dimensions on a rectangular mesh. The continuous vorticity field is represented by a cloud of closely spaced discrete vortices. The airplane wake appears initially as a line of closely spaced vortices that subsequently wrap up and form the tip vortices. Except for the concentrated tip vortices, the velocity field is calculated at the mesh points from the Poisson equation relating the stream function to the vorticity. The vorticity itself is evaluated by calculating the local concentration of the discrete vortex cloud. Turbulence is simulated by adding a random additional term to the circulation of each vortex element in such a way as to guarantee a Kolmogoroff spectrum as the mean. Fast Fourier Transform techniques are used to solve for the velocity field at each time step. The individual vortices are then moved appropriately in this velocity field.

A primary effect that is not coupled into the model at present, but which may be important at early time, is the axial motion. However, the axial flow does not affect directly the transport of the trailing vortex except when it is drastically

Received May 16, 1974; revision received Dec. 8, 1975. This work was sponsored by the NASA Marshall Space Flight Center under Contract NAS8-28984. The authors are greatly indebted to both R. M. Huffaker and H. Jeffries for their many suggestions and in-depth discussions.

Index categories: Aircraft Gust Loading and Wind Shear; Jets, Wakes, and Viscid-Inviscid Flow Interactions.

*Vice President.

†Staff Scientist. Now with Science Applications, Inc., La Jolla, Calif. Associate Member AIAA.

reduced. Until a quasi-three-dimensional approach is adopted, we shall not include this axial motion.

The LDV System is modeled by calculating the system response as the focal point is moved in range and elevation angle in the scan plane. When the system is focused at a given point in space, the Doppler spectrum response is calculated by considering contributions from each range point and superposing these, multiplied by a theoretical range response function. The velocity components are obtained from the hydrodynamical model at various times. A unique feature of the modeling of the hydrodynamics allows the tip vortices to be treated with high spatial resolution by invoking specific models of the core structure while at the same time retaining a lower resolution representation of the larger scale features. In the present analysis, we use Owen's model of the core structure and its decay. More accurate representations of the vortex structure are currently available[1,2] and can be included as required. The range response function is constructed from a previous analysis (in appendix of Ref. 3) of the optical system for Gaussian beams. Effects of finite truncation and blocking of the primary mirror have been treated by a detailed two-dimensional propagation analysis (not published). In the system model these effects are included by simply degrading the Gaussian beam analysis appropriately.

The spectrum is calculated by multiplying the aerosol density by the response function at each range point and cumulating this contribution in the appropriate velocity (or frequency) channel. The aerosol density in the neighborhood of the core is affected by centrifuging at late time, and a model for this has been developed (Appendix I in Ref. 4). However, in the present simulation calculations, a uniform particle density is assumed.

Once the spectrum has been evaluated, simulations of the data analysis procedure are carried out. Various moments of the spectrum (the mean velocity, variance, skewness and kurtosis) and certain other characteristics of the spectrum are calculated: the velocity of the highest channel above threshold (V_{peak}), the velocity of the channel having the peak signal (V_{max}), the signal level in this channel (I_{peak}). All of these data, in addition to the fundamental input (the value of the parallel velocity at the particular range point) are presented on a (three-dimensional) range-elevation angle plot. Also plotted are the actual locations of the vortex cores. The geometry of the simulated laser scan pattern together with the vortex wake motion are separately displayed. This entire procedure is repeated for each time step of interest.

In the following section we give a detailed description of the hydrodynamic model followed by a description of the laser doppler system simulation. Example results are given in Sec. V for a simulation of B747 and B720. Results of simulation of ground wind anemometers and acoustic systems are also presented.

II. Formulation of the Hydrodynamic Model

A. Numerical Procedure for the Inviscid Fluids

When the viscosity is negligible the vorticity equation takes the form

$$d\zeta/dt = -\nabla(1/\rho)\times\nabla p \tag{1}$$

and to first order in the density difference [since $p=\rho_0 g+\dot{0}(\nabla\rho/\rho)$],

$$d\zeta/dt = -(\nabla\rho/\rho_0)\times g \tag{2}$$

For the two-dimensional motion in the x, y plane the vorticity is effectively a scalar (i.e., has only a z component). Thus, for a vertical (y direction) downward gravitational acceleration g, Eq. (2) becomes

$$d\zeta/dt = (g/\rho_0)(\partial\rho/\partial x) \tag{3}$$

Of particular interest is the case of a stratified fluid. Here we divide the entire fluid into layers of slightly differing density. In this case, vorticity is generated only at the interface between the layers, the remainder of the flow remaining to be irrotational.

A convenient numerical analysis of the evolution of the fluid motion can be obtained by dividing up the interface into a number of discrete fluid elements and approximating the circulation of each element as being concentrated into a line vortex having circulation Γ_i.

The total circulation of a given (i^{th}) fluid element $\Gamma_i=\zeta_i dx'$ dy' is then determined by

$$\frac{d\Gamma_i}{dt} = \frac{g(\rho_+-\rho_-)}{\rho_0}\Delta y_i n_z \tag{4}$$

where ρ_+ is the density to the right of the interface and ρ_- that to the left. Δy_i is the separation between adjacent fluid elements on the interface and n_z is the unit vector perpendicular to the plane of motion. The evaluation of the fluid motion then reduces to the problem of following the motion of the individual discrete vortices. The velocity of the i^{th} vortex is a summation over contributions from all other vortices:

$$\frac{dr_i}{dt} = u_i = \sum_{j\neq i}^{N}\frac{\Gamma_i}{2\pi}\times\frac{(r_i-r_j)}{|r-r_j|^2} \tag{5}$$

This equation of motion plus the relation determining the circulation growth rate (Eq. 4) in which Δy_i is replaced by $\frac{1}{2}(y_{i+1}-y_{i-1})$ yields a direct deterministic procedure for following the motion.

Equation (4) is the basis for calculating the vorticity due to the buoyant exhaust and its subsequent variation, and Eq. (5) is the conventional Green's function formalism. In practice, Fast Fourier Transform techniques are applied to solve the stream function vorticity equation $\nabla^2\psi=\zeta$, Eq. (6). From the distribution of the discrete vortices, the continuous vorticity distribution is obtained by cumulating the vorticity in each cell. The vorticity due to each vortex is assumed to be smeared out uniformly over one mesh. This is a standard procedure for these types of mixed Lagrangian-Eulerian techniques. Once the vorticity field is obtained the Fourier components of the vorticity are then calculated. Fourier components of the stream function can be obtained from the Fourier transform of Eq. (6); that is

$$\psi_k = -\zeta_k/(k_x^2+k_y^2)$$

The velocity field can be obtained most accurately by simple multiplication in Fourier space, rather than direct finite differencing in physical space. Thus,

$$u_k = k\times\psi_k$$

Transforming back to physical space we find the velocity of each discrete vortex by a bilinear interpolation from the nearest four space mesh points. The position of the vortices can then be advanced through the next time step. The numerical method, utilizing the concept of discrete vortex elements moving on a fixed mesh space was dubbed the vortex-in-cell (VIC) method. Several applications of the method were discussed in Ref. 5.

B. Formulation of a Hybrid Vortex-in-Cell Method

The limitation of a purely FFT scheme, as discussed in Sec. A, is its small time step. This time is essentially determined by the peak angular velocity of the tip vortex. Since angular velocities exceeding 10 rad/sec are expected in some cases, the time step required to follow this motion would be substantially less than 0.1 sec. To cover an elapsed time of 100 sec requires more than 1000 steps. This is excessive, and it is desirable to obtain a numerical scheme that can handle the

same number of vortices without the limitations of a small integration time step.

For the present study, there is another reason that a purely FFT scheme will not be adequate. In order to resolve a vortex flowfield that has a core radius of a few meters, one must have a mesh smaller than the core radius. On the other hand, one must cover an overall dimension determined by the product of the wind speed and the total elapsed time of interest (several hundred meters). The ratio of this dimension to the core radius indicates that at least 100 mesh points in each direction are required to resolve the flowfield, and this is large even for the CDC 7600. To achieve an economical and accurate computation, we introduce a hybrid method that is capable of resolving the fine structure near the tip vortex while maintaining a relatively coarse mesh.

We utilize the fact that the vortex sheet quickly coagulates into two (or more) well-defined localized structures which maintain their identity for many rotations. The total velocity field is taken to be a superposition of two parts: one the contribution of the localized tip vortices, and the other due to the more distributed vorticity. The velocity field of the tip vortex is constructed from an axisymmetric model. This model in general requires values of two quantities to be specified: the total vortex circulation $\Gamma(t)$, and a characteristic radius R (typically the core radius). Both Γ and R are functions of time. In the present simulation we use the model constructed by Owen[6] for a turbulent vortex and for which $R=(2/\sigma)(vt)^{1/2}$ and $\sigma=(1/\Lambda)(v/\Gamma_0)^{1/4}$ where v is kinematic viscosity, Γ_0 is the total circulation over one wing, Λ is a numerical value of order unity (and is set equal to 1 in the present simulation). A simple laminar diffusion profile is used for the radial distribution of circulation. $\{\Gamma[1-\exp(-r^2/R^2)]\}$. As the core expands, the distributed vortices may be captured and incorporated into the tip vortices. The tip vortex locations are updated to the centroid of the original vorticity distribution in this capture process. The velocities due to the tip vortices and the wind shear are then superposed.

In practice, one avoids the short time step problem by superposing displacements rather than velocities. The angular displacements directly induced by the tip vortices are evaluated. This displacement is then added to that due to the slowly varying background velocity field. By repeating this process at each time step, one follows accurately the motion near the core even though a given point may rotate several times about the tip vortex during one time step.

C. Calculation of the Circulation of the Vortex Sheet

By wing theory, the lift or wing loading is linearly proportional to the circulation about the wing cross section, and it is well known that for simple high aspect ratio wings, the wing loading can be approximated by the elliptic curve

$$S(x)/S_0=[1-(x/R)^2]^{1/2} \tag{6}$$

where S_0 is the maximum circulation at $x=0$ and R is the wing span. The circulation between the point x and $x+dx$ is decreased by the amount $\Delta S=S(x+dx)-S(x)$ and this amount of circulation must be shed from the wing section between these two points. Thus, the circulation of the trailing vortex sheet at any point x is equal to the rate of change of $S(x)$, that is, $-dS(x)/dx$ along the wing.

To model this initial velocity field we divide the vortex sheet into a number of strips in the flight direction, each segment of which has a circulation $\Gamma_i(x)$ given by

$$\Gamma(x_i)=[S(x_i)-S(x_{i+1})]/\Delta x \tag{7}$$

where $\Delta x=x_{i+1}-x_i$.

Real lift distribution deviates considerably from the elliptic loading rule, as was pointed out by Donaldson et al.[2] Although the real profiles can be modeled easily in the present model, we will apply the elliptic loading rule for its simplicity.

D. Simulation of the Turbulent Wind Shear Field

The wind profile near the ground in a neutrally stable atmosphere is known to exhibit a logarithmic dependence upon the height y[7]

$$U=\frac{u_\tau}{\kappa}\ell n\left(1+\frac{y}{y_0}\right)+\text{constant}$$

where u_τ is the friction velocity and is usually related to the wind velocity by the relation $u_\tau\cong 1/30U$ (at standard height). The parameter κ is the Karman constant[8] and is equal to 0.42. The parameter y_0 is the roughness height.

From the preceding equation the vertical wind shear can be obtained by taking the derivative with respect to y

$$\zeta(y)=u_\tau/\kappa y$$

To describe the mean wind-shear field, this circulation is assigned to a uniform distribution of discrete vortices as follows

$$\Gamma_0=\frac{U_\tau}{\kappa}\ell n\left(1+\frac{\Delta y}{2y_0}\right)\Delta x$$

for ground layer and

$$\Gamma_j=\frac{U_\tau}{\kappa}\ell n\left(\frac{Y_j+\Delta y/2}{Y_j-\Delta y/2}\right)\Delta x \qquad j=2,\ldots,N \tag{8}$$

for layers about ground, where Δx, Δy are the horizontal and vertical mesh sizes, N is the total number of rows of vortices, and $N=17$ for the study. The present treatment is similar to that of Brashears and Hallock[9] except for the number of wind shear vortices used to simulate the wind-shear field. In the present analysis, the introduction of the mixed Eulerian-Lagrangian coordinates (a particle-in-cell method) allows a highly detailed spatial resolution of the wind field at relatively modest cost.

The mean wind profile is assumed prescribed at time $t=0$ and is independent of horizontal location. To simulate the turbulence we seek a realization of the turbulent wind field assuming the Kolmogoroff-5/3 law applies and the dissipation rate is constant throughout the flowfield. In essence, the turbulence is assumed to be represented by constructing, at time $=0$, a random field of vortices with the fluctuating velocity field satisfying the Kolmogoroff law (in expectation).

Let the fluctuating velocity component be represented by a Fourier series

$$u(x)=\sum\sum_{k=0} u(k)\exp(ik\cdot x), \quad k=(k_x,ky)$$

where the $u(k)$ is the Fourier component of the $u(x)$. A specific realization can be determined from

$$|u(k)|=-<u(k)>\ell n(1-r_1)$$

or

$$=-\left(\int\int_{k-(\Delta k/2)}^{k(\Delta k/2)}\frac{c\epsilon^{2/3}k^{-8/3}}{2\pi}dk_x dk_y\right)^{1/2}\ell n(1-r_1)$$

where r_1 is an equidistributed random number in (0,1) and $k=(k_x^2+k_y^2)^{1/2}$, $c\cong 1.52$ and ϵ is the dissipation rate. Since $u(k)$ is in general complex, a random phase must also be introduced; this yields

$$u(k)=-\left[\int\int_{\Delta k}\frac{c\epsilon^{2/3}k^{-8/3}}{2\pi}dk_x dk_y\right]^{1/2}\ell n(1-r_1)\exp(i2\pi r_2)$$

where r_2 is also an equidistributed random number in (0,1). Taking curl of this relation in x space, the vorticity is obtained and the circulation strength of each vortex can be calculated by integrating over the mesh $\Delta x \Delta y$

$$\Gamma(x) = F^{-1}\left\{2i[u(k)k_x - v(k)k_y]\frac{\sin(k_x\Delta x/2)}{k_x}\frac{\sin(k_y\Delta y/2)}{k_y}\right\} \quad (9)$$

where Δx, Δy are the mesh sizes and F^{-1} represents the inverse Fourier transform.

This circulation is added to the time independent wind shear given by Eq. (8) at initial time, the subsequent motion is then determined by the interactions among the vortices.

III. Spectral Signal Characteristics for Coaxial LDV Systems

Characteristics of NASA/MSFC LDV systems are described in detail by Krause et al.[10] and Wilson et al.,[11] here we are concerned only with the parameters relevant to the simulation of spectral response.

A. Signal-to-Noise Ratio

Coherent heterodyne laser detection systems are commonly operated in a slot noise limited condition; that is, the noise is determined entirely by the number of scattered photons detected, not by the receiver electronics. The performance of a general coherent laser system detecting the radiation scattered from a continuously distributed aerosol has been analyzed previously. In the present case of a coaxial system (that is, the received scattered signal is collected through the transmitting optics), the signal-to-noise ratio is given by[3]

$$S/N = \frac{\eta P_\omega}{2\Delta\omega}\left(\frac{\lambda}{\pi\gamma}\right)^2 \int_0^\infty \frac{\overline{n_f\sigma}(L)}{(L-L^*)^2+\Delta L^2}\,dL \quad (10)$$

Here $\overline{n_f\sigma}$ is the differential backscattering cross-section per unit range per steradian, η the overall loss factor (atmospheric absorption, optics and electronics), P_ω the transmitter power that is scattered into the bandwidth $\Delta\omega$ (i.e., $P_\omega\Delta\omega$ is proportional to the number of photons transmitted that would be scattered into the frequency interval $\Delta\omega$ in an ideal system). We have assumed that both transmitter and receiver have a Gaussian apodization with radii R_t and R_r, respectively, at the e^{-2} intensity points. The transmitted wave fronts are focused at a range f_t and the receiver section is focused at f_r. The focal point for the receiver is determined by locating the position of the virtual image of the local oscillator. In terms of these optics parameters, the various parameters in Eq. (10) are given by the relations

$$\gamma = (\theta_{\text{geom}}^2 + \theta_{\text{diff}}^2)^{1/2}$$

$$\theta_{\text{geom}} = (R_r^2 + R_t^2)^{1/2}/f_2$$

$$\theta_{\text{diff}} = \lambda(R_T^2 + R_r^2/R_tR_r)^{1/2}$$

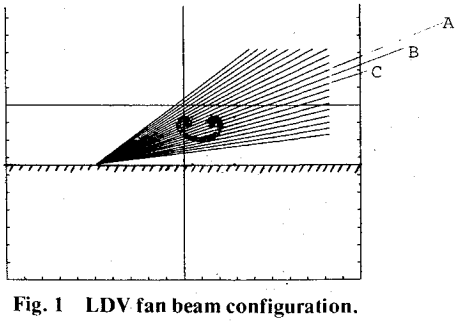

Fig. 1 LDV fan beam configuration.

$$f_l = \left(\frac{R_r^2}{f_r} + \frac{R_t^2}{f_t}\right)\Big/\left(\frac{R_r^2}{f_r^2} + \frac{R_t^2}{f_t^2}\right)$$

$$f_2 = \left[\frac{R_t^2+R_r^2}{(R_r^2/f_r^2)+(R_t^2/f_t^2)}\right]^{1/2}$$

$$L^* = \frac{f_l}{1+(\lambda f_2/\pi R_tR_r)^2}$$

λ is the wavelength and is equal to 10.6μ for NASA/MSFC LDV system, and

$$\Delta L = \left\{\left[\frac{\lambda f_l/\pi R_tR_r}{1+\left(\frac{\lambda f_2}{\pi R_tR_r}\right)^2}\right]^2 + \frac{\left[\frac{R_rR_t}{(R_r^2+R_t^2)}\left(\frac{f_2}{f_t}-\frac{f_2}{f_r}\right)^2\right]}{\left[1+\left(\frac{\lambda f_2}{\pi R_tR_r}\right)^2\right]}\right\}^{1/2} f_2$$

When the atmospheric backscattering properties of the doppler signal vary negligibly across the depth of field $\pi\Delta L$, the signal-to-noise ratio takes the form

$$S/N = \frac{\pi}{2}\frac{\eta P_\omega}{\Delta\omega\Delta L}\left(\frac{\lambda}{\pi\gamma}\right)^2\overline{n_f\sigma}\left(\frac{1}{2}+\frac{1}{\pi}\tan^{-1}\frac{L^*}{\Delta L}\right) \quad (11)$$

In order that significant range resolution be achieved, the aperture must be chosen so that ΔL is small compared to L^*, i.e., so that the scattering particles are well within the near field ($\lambda f/\pi R^2 << 1$). In this limit, the signal-to-noise is independent of range

$$S/N = \eta\frac{P_\omega}{\Delta\omega}\overline{n_f\sigma}\frac{\lambda}{4} \quad (12)$$

and the range resolution (the region from which comes half the scattered energy) is

$$\pi\Delta L = \lambda L^2/R^2 \quad (13)$$

The signal-to-noise given in Eq. (10) represents a mean value averaged over the bandwidth $\Delta\omega$. When the receiver channel width exceeds the doppler width of the scattered signal, $\Delta\omega$ is to be set equal to the receiver channel bandwidth. When the doppler spread is large enough to cover more than one receiver channel, $\Delta\omega$ is to be set equal to the doppler width of the incoming signal. In this case, the signal-to-noise is independent of the individual received channel bandwidths.

When the magnitude of the scattered power changes only slightly in a time equal to the reciprocal of the individual receiver channel bandwidths, further improvement in the signal-to-noise ratio can be achieved by incoherent integration of the power level at the output of the receiver channels. The increase is essentially equal to $(\Delta\omega_c\tau_i)^{1/2}$, where τ_i is the allowed integration time and $\Delta\omega_c$ the receiver channel bandwidth.

For optimum performance, the integration time should be matched to the dwell time. In the NASA/MSFC LDV system, the receiver channel width is 100 kHz, and dwell times range from 1 to 10 msec, yielding potential increases in signal-to-noise of factors of 3-10.

B. Spectral Response

A typical configuration for a single LDV system is shown in Fig. 1. In the scan plane there are 21 beams at 1.5° apart, each covering a range between 60 and 250 m. Superimposed in the

same figure is the location of the trailing vortex sheet. The flow velocity along each line of sight, (parallel velocity $V_\parallel$) are presented in Fig. 2. These plots would indicate the response of an LDV system that had infinitely high range resolution. At large lateral separations from the vortices, that is, at the top and bottom of the figure, only a very weak velocity perturbation is seen. As the line of sight gets closer to the vortex, the velocity peaks at the vortex location (C). However, if the line of sight passes directly through the vortex only a small component of velocity parallel to the line of sight is obtained. (B). Lines of sight which pass between the vortex pair sense both vortices (A). The peak value of the parallel velocity changes sign as the line of sight crosses the vortex center and maximizes at the edges of the core.

The finite range resolution as defined by Eq. (13) smears out this velocity profile to a greater or lesser extent depending on range. The LDV system senses the doppler spectrum as averaged over the range response function of the instrument. Various moments or mean properties of the velocity spectrum may be calculated from the relation

$$\overline{f(s,\theta)} = \int^{\infty} f(V_\parallel) I(s,\theta,V_\parallel)\,dV_\parallel \Big/ \int I(s,\theta,V_\parallel)\,dV_\parallel$$

where $I(s,\theta,V_\parallel)$ is the doppler spectral intensity, S is range, θ is elevation angle. This intensity in turn depends on the atmospheric backscattering properties and the range response function $g_s(s,s')$. For Gaussian aperture apodization, the range response function has the form

$$g_s(s,s') = \left[1+4\left(\frac{s-s'}{Rs}\right)^2\right]^{-1}$$

where Δs is the range resolution (between 3db points) obtained by multiplying Eq. (13) by 2:

$$(\Delta s)_{\text{Gaussian}} = 2(\lambda/\pi)(s/R)^2$$

Here s is the range to the focal point and R is the aperture radius (e^{-2} intensity). To account for finite truncation of the telescope mirror in the simulation model, we simply degrade the resolution by a fixed factor

$$\Delta s = 2f(\lambda/\pi)(s/R)^2 \tag{14}$$

Detailed propagation calculations (not published) have been carried out to examine the effects of finite apertures and blocking of the mirror. For a Gaussian beam truncated at the e^{-2} radius, f is computed to be 2.1.

Two modes of operation are possible, in general: one where the sign of the doppler shift is sensed and the other where only the magnitude is used. All of the calculations presented here assume the latter mode, although either or both modes can be implemented.

The calculation of the spectrum begins with the parallel velocity profile vs range. When the system is focused at the range s, the spectrum level in the velocity channel V_k is obtained from a finite difference representation of

$$I(s,\theta,V_k) = I_0 \int_0^{\infty} \frac{\overline{n\sigma}(s')\,g_v(V_\parallel(s') - V_k)\,ds'/\Delta s}{\pi[1+4(s-s')/\Delta s)^2]}$$

Here $g_v(\delta V)$ is the frequency response of the filter and is taken to have the form

$$g_v(\delta V) = [1+(2\delta V/\Delta V)^{2p}]^{-1}$$

where ΔV is the velocity resolution (0.545 mps in the current simulation) and p is a parameter. The value $p=1$ gives a reasonable representation of the actual filter function in the NASA/MSFC system whereas $p\to\infty$ gives the square box filter. No great differences are expected between different values of p. The current demonstration calculations have all assumed $p=\infty$.

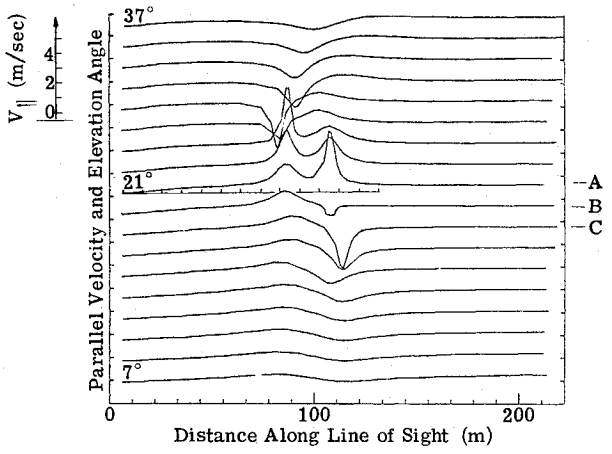

Fig. 2 r,θ-plot for the parallel velocity ($V_\parallel$).

Analyses of aerosol size distribution in continental air and centrifugal effects near the vortex core are discussed in Thomson and Meng.[4] Here we only point out that the time t_l for centrifugal effects to substantially alter the local backscattering cross section within the vortex core can be represented by the following relation:

$$t_l = \left(\frac{2\pi a_0}{\lambda}\right)^2 T_0 = 88.8\frac{\rho_a}{\rho_p}\frac{v}{\lambda^2}\left(\frac{2\pi R^2}{\Gamma}\right)^2$$
$$= 1.185\times 10^4\left(\frac{2\pi R^2}{\Gamma}\right)^2 \text{sec} = 1.176\,T(a=2\mu)$$

For small high-velocity cores, these centrifuging times are relatively short. (For a B707, t_l is 10 sec or less for core diameters less than about 10 ft). Thus, small high-speed core may be visible as an enhancement of the scattering around the periphery of the vortex.

IV. General Description of LDV Simulation Code

A model of the hydrodynamic and laser system described in the preceding sections is formulated as a numerical computer program. This program calculates as a function of time the response of a pair of LDV scanning systems which view the region below and near the aircraft track. Each system is described by a prespecified number of equally spaced lines of sight that uniformly cover elevation angles between a given maximum and minimum value. In the present formulation, the program "tracks" the wake, locates the elevation angle of the midpoint between the two tip vortices, and automatically centers the elevation angle scan on this point. At regularly spaced time intervals, the simulated LDV system response is calculated as a function of range (to some maximum range) for each elevation angle.

The output of the program is displayed in a series of plots. The vortex sheet shed from the aircraft wing, as well as the tip vortices are first presented on an $x-y$ plot along with the locations of all the distributed wind shear vortices. The LDV system configuration is displayed by superposing individual lines of sight of the two beams on a plot of the vortex sheet location.

The LDV system response is calculated from the distribution of the parallel wind velocity component along each line of sight. Before presenting simulations of the system response, a high resolution "three-dimensional" plot of this parallel velocity component is presented. This is the basic quantity sensed by all doppler radar backscatter systems (laser, acoustic, or microwave). Here the velocity is plotted vs range for each elevation angle and an entire scan frame is presented in a single range-elevation angle plot. Curves for different elevation angles are displaced in the vertical direction by an amount proportional to the angle.

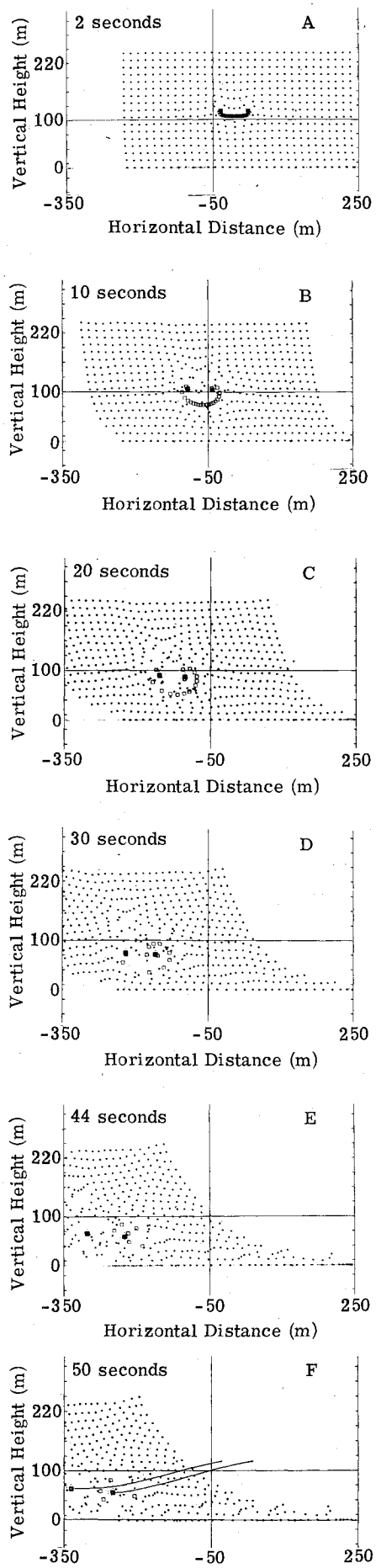

Fig. 3 Trailing vortex configurations at 2, 10, 20, 30, 44, and 55 sec.

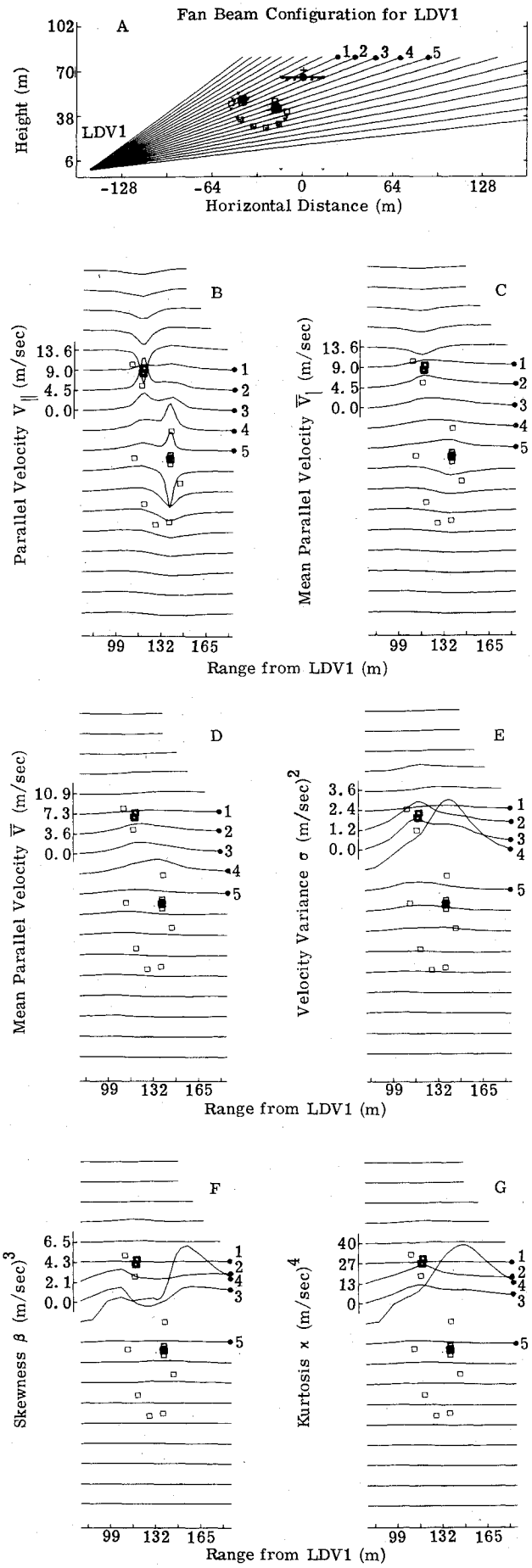

Fig. 4 Fan beam configuration and distributions of spectral moments along various lines of sight for LDV1 located at mean range to wake: 120 m (B-720 simulations at 18 sec).

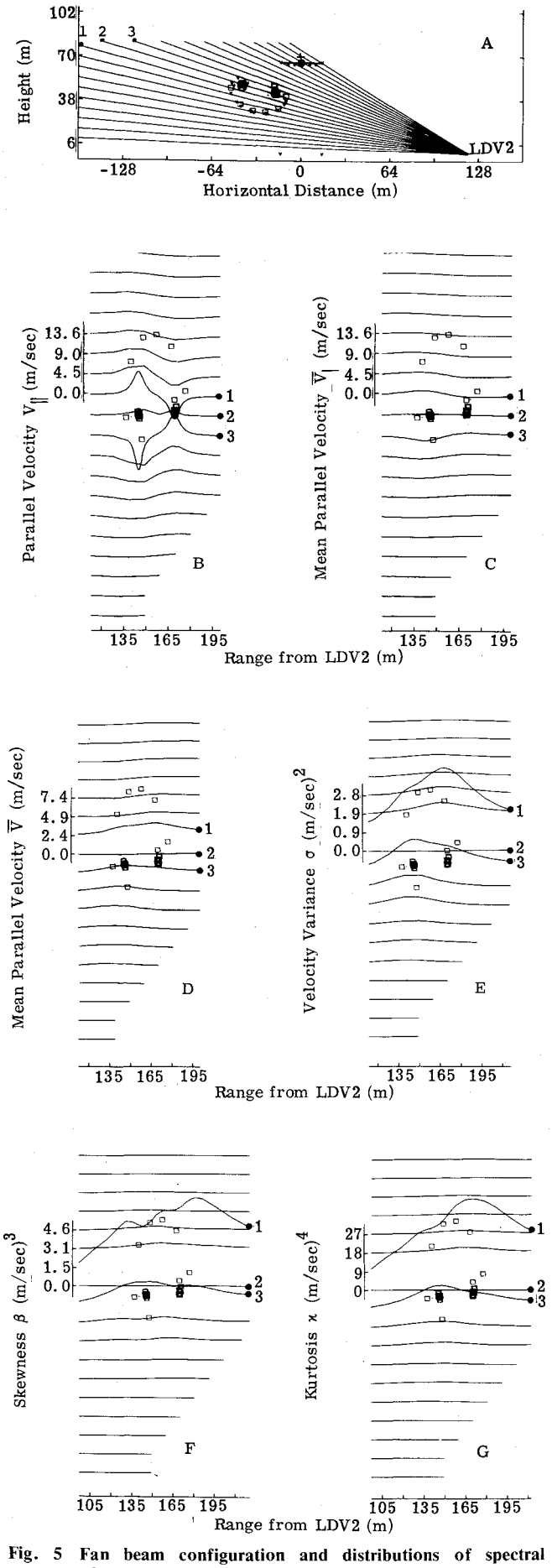

Fig. 5 Fan beam configuration and distributions of spectral moments along various lines of sight for LDV2 located at mean range to wake: 160 m (B-720 simulations at 18 sec).

The doppler spectral intensity $I(V)$ is then calculated (according to the prescription in Sec. III) at each point in space. Because of the large amount of data, only samples of these spectra at selected elevation angles are presented.

After the spectrum is computed, a number of spectral moments are determined. At present there are ten different variables or moments that are calculated at each range-elevation point. These are:

1) The parallel velocity $V_\parallel$: the actual component along the line of sight as computed directly from the hydrodynamic model.

2) The (unrectified) mean parallel velocity ($\bar{V}_I$): this is the parallel velocity simply averaged over the theoretical range resolution function

$$\bar{V}_I(s) = \int_0^\infty g_s(s-s')\, V_\parallel(s')\,ds' \Big/ \int_0^\infty g_s(s-s')\,ds'$$

3) The (rectified) mean parallel velocity $\bar{V}$: this is the parallel velocity as sensed by the LDV system with finite range resolution

$$\bar{V} = \sum_{|V_k|>V_0} [I(k) - I_0(k)]\,|V_k|\,/I_{\text{sum}}$$

Here V_k is the velocity of the kth channel, $I(k)$ the computed intensity in this channel, $I_0(k)$ a threshhold intensity level (to be discussed subsequently), and V_0 a velocity threshhold. I_{sum} is the total intensity in all channels (above threshhold)

$$I_{\text{sum}} = \sum_{|V_k|>V_0} (I(k) - I_0(k))$$

In all moment calculations, no contribution is included for intensities below a given intensity threshold (i.e., only nonzero contributions for $I(k) > I_0(k)$ are allowed). In this computation the system is assumed incapable of distinguishing positive from negative doppler frequencies.

4) The velocity variance σ

$$\sigma = \left[\sum_{|V_k|>V_0} (|V_k| - \bar{V})^2 (I(k) - I_0(k))/I_{\text{sum}} \right]$$

5) The skewness β

$$\beta = \sum_{|V_k|>V_0} (|V_k| - \bar{V})^3 (I(k) - I_0(k))/I_{\text{sum}}$$

6) The kurtosis κ

$$\kappa = \sum_{|V_k|>V_0} (|V_k| - \bar{V})^4 [I(k) - I_0(k)]/I_{\text{sum}}$$

7) The peak velocity (V_{peak})

The velocity of the highest frequency channel having a spectral intensity exceeding the threshhold value (and if $V_{\text{peak}} > V_0$).

8) The velocity of the maximum intensity ($V_{\max}$)

The velocity of the channel having the highest value of $I(k) - I_0(k)$ and for which $V_k > V_0$.

9) The maximum intensity (I_{peak})

The total signal strength above the intensity and velocity thresholds

The largest value of $I(k) - I_0(k)$ for all velocities greater than V_0.

10)Sum of intensity (I_{sum})

$$I_{sum} = \sum_{|V_k|>V_0} [I(k) - I_0(k)]$$

All of these quantities are presented in the range-elevation angle plots described previously. To illustrate the relationship between the variations of each variable and the tip vortices, we have also superposed on the plots the location of the vortex sheet and the tip vortices.

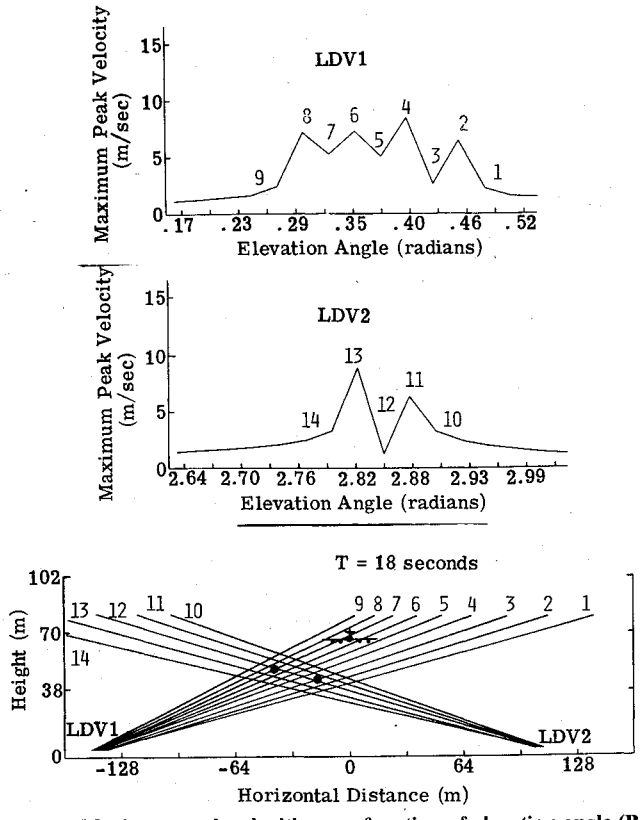

Fig. 6 Maximum peak velocities as a function of elevation angle (B-720 simulation at 18 sec).

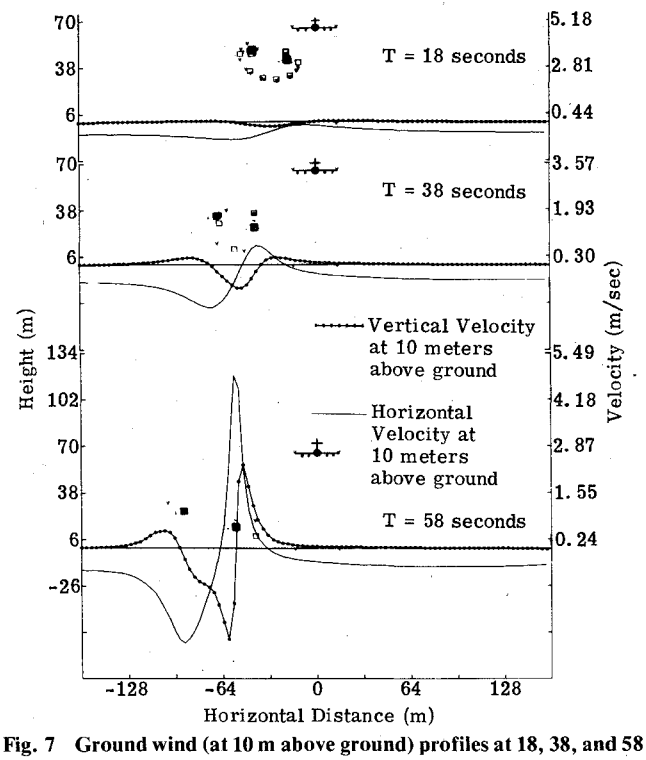

Fig. 7 Ground wind (at 10 m above ground) profiles at 18, 38, and 58 sec (B-720 simulation).

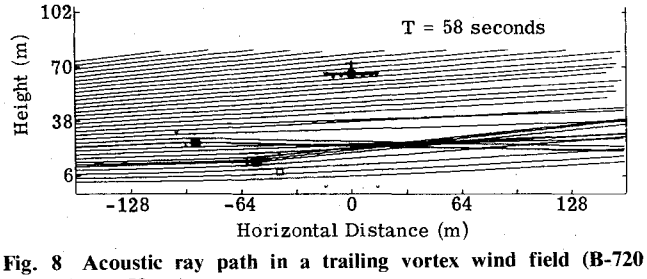

Fig. 8 Acoustic ray path in a trailing vortex wind field (B-720 simulation at 58 sec).

V. Results and Discussion

A. B-747 Simulation

A simulation of the trailing vortex wake of a Boeing 747 aircraft at a height of 120 m above the runway using a 32×32 grid was carried out. Figure 3(A) shows the vortex sheet is represented by 25 discrete vortices distributed over half the wing span, each is assigned a circulation according to Eq. (7). The wind shear vorticity is distributed over the flow domain on a 17×32 mesh, and the ground images (not shown) are obtained by the symmetry condition in the vertical direction. A single cylindrical region under each wing can be used to represent the engine exhausts. Circulation may be ascribed to the 25 vortices outlining this region to simulate the effect of buoyancy. However, no buoyancy is actually present in any of the simulations presented in this report.

Figure 3 shows the overall picture of the vortex system at times up to 50 sec. At late time the wind shear vortices near the ground where the vorticity is maximum are swept up by the vortex wake and effects of the interaction between the wind shear and the tip vortices may be expected to appear. In Fig. 3(E), a tilting of the two vortices becomes apparent at time $t=44$ sec. The trailing vortices are transported nearly 300 m to the left from the original position, and the position of the wind shear vortices delineate clearly the wind profile.

B. B-720 Simulation

Figures 4 and 5 show simulations of the vortex wake of a B-720. The altitude at time zero was taken to be 55.3 m and the total circulation of one wing is 190 m^2/sec. A light wind was assumed according to $u_{wind}=0.5\ln(1+y/2)$ mps. Two LDV systems were assumed located on opposite sides of the aircraft track. Figures 4(A) and 5(A) show the overall geometry at an elapsed time of 18 sec for both LDV1 and LDV2. In Figs. 4(B) to 4(G) and 5(B) to 5(G), we show range-elevation plots of the following series of variables: $V_{\|}, \bar{V}_{|}, \bar{V}, \sigma, \beta, \kappa$. In all cases to be discussed, the intensity and velocity thresholds were taken to be zero. Five particular lines of sight are identified in Fig. 4 and exhibit various characteristics of the signature. In general, both vortices can be identified (at least at this range) in all lines of sight that pass between the two vortices. The line of sight 3 passes near the midpoint and shows two comparable peaks in Figs. 4(B) and 4(F). Lines of sight passing near the edge of a vortex core (but not through the core) show a strong peak (e.g., lines 2 and 4); however, when the line of sight passes directly through a vortex core (e.g., line 1), only the broad maxima from the other vortex is discernible. These features are particularly marked in the higher moments of velocity (that is, σ,β and a in Fig. 4(E-G) where the core edges are quite visible in line 4; whereas, the line of sight 1 passing through the core center shows no signature.

By comparing Figs. 4(B) to 4(C) of the line of sight 5, the effect of finite range resolution can be seen. Similarly, by comparing Figs. 4(C) to 4(D) of the same line, effect of rectification can be demonstrated. Signatures for all variables, except for $V_{\|}$ in Fig. 4(B), which has infinite range resolution, are confined in the region between the vortices. Only two angle separations (3°) away from the vortices the signature becomes invisible. The visibility of signature increases with the order of moment of velocity, and angle resolution also improves with higher velocity moments. The spread in range, however, is a function of range resolution only; using higher moments does not reduce it. Although it is not clearly shown here, the skewness becomes negative at close range (less than 120 m) on lines connecting two vortices.

Figure 5 shows the signatures as seen by the second LDV system (LVD2) at 18 sec after fly-by. The mean range to wake is about 160 m. Due to the coincidental alignment of the lines of sigl.. to that connecting the two vortices, it is not possible to separate out the two vortices angle-wise. Line of sight 2 in Fig. 5 shows there is no discernible signature for all variables, while lines of sight 1 and 3 show clear signatures. The signatures of the vortices are practically merged together at this range ($\sim$160 m) even though there are several peaks in Fig. 5(D-G).

More detailed discussions and simulations of other aircrafts and wind conditions are included in Ref. 4.

When plotted vs elevation angle, the maximum peak velocity V_{peak} for each line of sight identifies the core edges. Therefore, by drawing a line of sight at the angle corresponding to that of the maximum V_{peak} from each LDV system, it was conceived possible to locate the vortex at the intersection point. Figure 6 shows the maximum V_{peak} vs angle plots for LDV1 and LDV2. A selected set of lines of sight are indicated for each LDV system. In general, maxima are at lines of sight passing near the core edges (2, 4, 6 and 8 for LDV1 and 11, 13 for LDV2); minima are at lines of sight which pass through the core (3, 7 for LDV1 and 12 for LDV2) or away from it (1, 5, 9 for LDV1 and 10, 14 for LDV2). In practice, it is not always possible to identify all the peaks and troughs and, worse still, the signatures due to two vortices may merge together so that it is difficult to determine whether the peaks are due to one vortex or two. Another difficulty for this tactic is that the lateral spacing between lines of sight at this range ($\sim$160 m) is too large to define the structure of the core.

Although the primary purpose of this study is to analyze the LDV system responses, characteristics of two other systems, i.e., the ground-wind anemometers and acoustic systems can also be discussed in the framework of the present hydrodynamic model. Basic physics of these systems are described by Hallock et al.[12] We merely discuss the sample outputs by the present model. The Fig. 7 series show both the horizontal and vertical velocities at 18, 38, and 58 sec after flyby. Both initial aircraft position and trailing vortices are indicated. The velocity scale is shown on the right-hand side and varies as a function of time. Because of the skewness at 58 sec, the signal due to the upwind vortex is significantly stronger than the downwind vortex. The maxima of horizontal velocity correlates well with the real vortex location even when there is nonlinear wind shear interactions. The breadth of the upwind vortex signal is quite narrower than the downwind vortex one, and minima spacing of the anemometers should be determined from these breadths.

An acoustic ray path plot is shown in Fig. 8. Because of the flow rotation, the rays are refracted downward by the downwind vortex and upwards by the upwind vortex. Refraction near the ground is due to the wind shear. It may be significant when wind shear is strong. Outputs of this simulation code can serve as a guideline for interpreting the flight data.

VI. Conclusions

Two vortex detection modes may be considered: a local "hard target" mode in which a direct signal is obtained from the vortex centers and a "soft target" mode in which a portion of the flowfield pattern is detected and the location of the vortices deduced by some sort of pattern recognition procedure. The former has the advantage of being simple and unambiguous, but may be subject to missed targets and/or false alarms. The latter requires a theoretical model for implementation and may be less able to provide precise position information. However, in general it tends to be less subject to misses or false alarms.

In order to be able to evaluate optimal detection modes, we have attempted first to generate a simulation of the vortex-atmosphere hydrodynamics together with a simulation of the response of the laser doppler sensor system.

Several conclusions may be drawn from examination of the simulation data and comparison with the flight data:

1) The vortex wake appears as a spatially-distributed target, particularly for the low-order moments. The vortex center itself provides a null signal to the LDV sensor and accurate location depends on locating the core edges or establishing the origin of the spatial pattern.

2) The range resolution varies strongly with range and the individual vortices are seen separately in the simulation at short range (ranges less than 120-150 m) but at long range (greater than 200 m) both vortices are merged.

3) At the longer ranges, high order moments give the best range and angle location. The kurtosis appears to yield the best localization of the technique considered.

4) The angular spacing (1.5°) presently used is inadequate to resolve the vortex at long range, and simulations of spatial signatures by using the unrectified velocity $\bar{V}_l$ should be carried out.

References

[1] Betz, Z., "Behavior of Vortex Systems," NASA TM 713, 1933.

[2] Donaldson, C. duP., Snedeker, R. S., and Sullivan, R. D., "Calculation of the Wakes of Three Transport Aircraft in Holding, Takeoff, and Landing Configurations, and Comparison with Experimental Measurements," Air Force Office of Scientific Research, Washington, D. C., AFOSR-TR-73-1594 (also FAA-RD-73-42), 1973.

[3] Thomson, J. A. L. and Meng, J. C. S., "A Feasibility Study for the Detection of Upper Atmospheric Winds Using a Ground Based Laser Doppler Velocimeter," PD-75-042, March 1975, Final Report for Contract NAS8-28984, Physical Dynamics, Inc., Berkeley, Calif.

[4] Thomson, J. A. L. and Meng, J. C. S., "Laser Doppler Velocimeter System Simulation for Sensing Aircraft Wake Vortices. Part I. Simulation Model." PD-74-058, Dec. 1974, NASA-CR-120624, N75-18265, Physical Dynamics, Inc., Berkeley, Calif.

[5] Thomson, J. A. L. and Meng, J. C. S., "Studies of Free Buoyant and Shear Flows by the VIC Method." *Proceedings of the Fourth and Shear Flows by International Conference on Numerical Methods in Fluid Dynamics, Lecture Notes in Physics,* Vol. 35, pp. 403-416, 1974.

[6] Owen, P. R., "The Decay of a Turbulent Trailing Vortex," *Aeronautical Quarterly*, Vol. 21, pp. 69-78, 1970.

[7] Blackdar, A. K. and Tennekes, H., "Asymptotic Similarity in Neutral Barotropic Planetary Boundary Layers," *Journal of the Atmospheric Sciences*, Vol. 25, pp. 1015, 1968.

[8] Hinze, J. O., *Turbulence*, McGraw-Hill, New York, 1959.

[9] Brashears, M. R. and Hallock, J. N., "Aircraft Wake Vortex Transport Model," AIAA Paper 73-679, Palm Springs, Calif., 1973.

[10] Krause, M. C., Morrison, L. K., Craven, C. E., Logan, N. A., and Lawrence, T. R., "Development of Theory and Experiments to Improve Understanding of Laser Doppler Systems." Final Report to Contract NAS8-25921, LMSC-HREC TR-D306632, June 1973.

[11] Wilson, D. J., Krause, M. C., Coffey, E. W., Huang, C. C., Edwards, B. B., Shrider, K. R., Jetton, J. L., and Morrison, L. K., "Development and Testing of Laser Doppler System Components for Wake Vortex Monitoring. Vol. I. Scanning Development, Laboratory and Field Testing and System Modeling." Final Report to Contract NAS8-29824, LMSC-HREC TR-D390159-I, Aug. 1974.

[12] Hallock, J.N., Wood, W.D., and Spitzer, E.A., "The Motion of Wake Vortices – The Terminal Environment." 6th Conference on Aerospace and Aeronautical Meteorology, Nov. 12-15, 1974, El Pas, Texas, Published by AMS.